

Magmatic activity at the slowest spreading rates: insights from a high-resolution earthquake catalog obtained from Gakkel Ridge Deep (Arctic Ocean)

David Essing  *1,2, Annika Hellbrück  1,3, Vera Schlindwein  1,3

¹Alfred-Wegener-Institute, Helmholtz Centre for Polar and Marine Research, Bremerhaven, Germany, ²Institute for Geology Mineralogy and Geophysics, Ruhr University Bochum, Germany, ³Faculty of Geosciences, University of Bremen, Germany

Author contributions: *Conceptualization:* DE. *Data Curation:* VS. *Formal Analysis:* AH, VS. *Funding Acquisition:* DE, VS. *Investigation:* DE, AH. *Methodology:* DE. *Software:* DE. *Supervision:* VS. *Visualization:* DE, VS. *Writing – original draft:* DE, VS. *Writing – review & editing:* DE, AH, VS.

Abstract At the eastern end of Gakkel Ridge, Arctic Ocean, spreading rates drop below 5 mm/y near the termination of the active mid-ocean ridge in the Laptev Sea. A small-scale ocean bottom seismometer network deployed for one year at a volcanic center near Gakkel Ridge Deep in sea ice covered waters revealed abundant microseismicity despite the low spreading rate. In order to reveal spreading processes, we analyze a manually picked earthquake catalog refined by low-magnitude events detected by template matching. We attribute seismicity occurring randomly in time and space to tectonic stress release along the ridge. During short periods of hours to days, seismicity is organized in time and densely clustered in space with signs of migration away from an aseismic area. In analogy to volcanic centers at Knipovich Ridge and in Iceland, we interpret this organized seismicity as signs of ongoing localized magmatism occurring even at the slowest spreading rates.

Non-technical summary Volcanic eruptions at the seafloor largely go undetected although a long chain of volcanoes continuously creates new seafloor where tectonic plates drift apart at mid-ocean ridges. When the plate separation rate is very slow, volcanism cannot fill anymore the gap between the diverging plates, and we lack an understanding of how new seafloor is constructed in absence of sufficient volcanism. The slowest seafloor spreading globally happens at Gakkel Ridge in the Arctic Ocean, but it is challenging to study due to the persistent sea ice cover. We recorded earthquake activity near a potential volcano at 4000 m water depth using ocean bottom seismometers, a previously unattempted effort due to the high risk of instrument loss related to sea ice coverage. We analyzed the earthquake activity in time and space down to very low magnitudes finding two contrasting forms: tectonic earthquakes occurring scattered in time and space along the ridge and intense swarms of weak earthquakes for few hours duration, closely resembling the seismicity preceding recent volcanic eruptions in Iceland. We therefore argue that even at the slowest spreading rates, volcanism contributes to the formation of new seafloor.

Production Editor:
Gareth Funning
Handling Editor:
Lise Retailleau
Copy & Layout Editor:
Théa Ragon

Received:
May 24, 2024
Accepted:
February 23, 2025
Published:
March 6, 2025

1 Introduction

New oceanic crust is formed at mid-ocean ridges through the interplay of tectonic and magmatic processes. At the slowest spreading rates (< 20 mm/y), little melt is present, and tectonic processes play a major role (Cannat et al., 2006; Sauter et al., 2013). They manifest themselves in earthquakes, some of which are strong enough to be registered on land (Bergman and Solomon, 1990; Escartín et al., 2008), while the weaker seismicity associated to magmatic processes usually remains undetected unless local ocean bottom seismic networks are installed (Tolstoy et al., 2006). However, strong earthquake swarms including multiple events with $M > 4$ recorded onshore are known from slow-spreading ridges and have been interpreted as indicators of magmatic activity (Cesca et al., 2023; Müller and Jokat, 2000; Schlindwein, 2012; Schmid et al., 2017;

Tolstoy et al., 2001). Modelling suggests, that tensile crack opening caused by the advancement of the dike tip results in very weak seismicity (Rubin and Gillard, 1998). The observed strong swarm events, in contrast may rather indicate triggered faulting above the dike as the terrain subsides or other adjustments to the dike-induced changes in the stress field occur. Recent multi-disciplinary data sets from diking and eruption episodes in Iceland show that migrating, low magnitude ($M < 4$) seismicity indicates the advance of an intruding dike tip, while the widening of the dike may happen aseismically (Ágústsdóttir et al., 2019, 2016). Sigmundsson et al. (2022, 2024) show a complex interplay between tectonic and magmatic processes specific to the individual tectonic setting, with the diking triggering the release of preexisting stress in $M > 5$ earthquakes that precede recent eruptions in the trans-tensional stress regime of Reykjanes Peninsula. Due to the observational difficulties, the rare observations of submarine

*Corresponding author: david.essing@rub.de

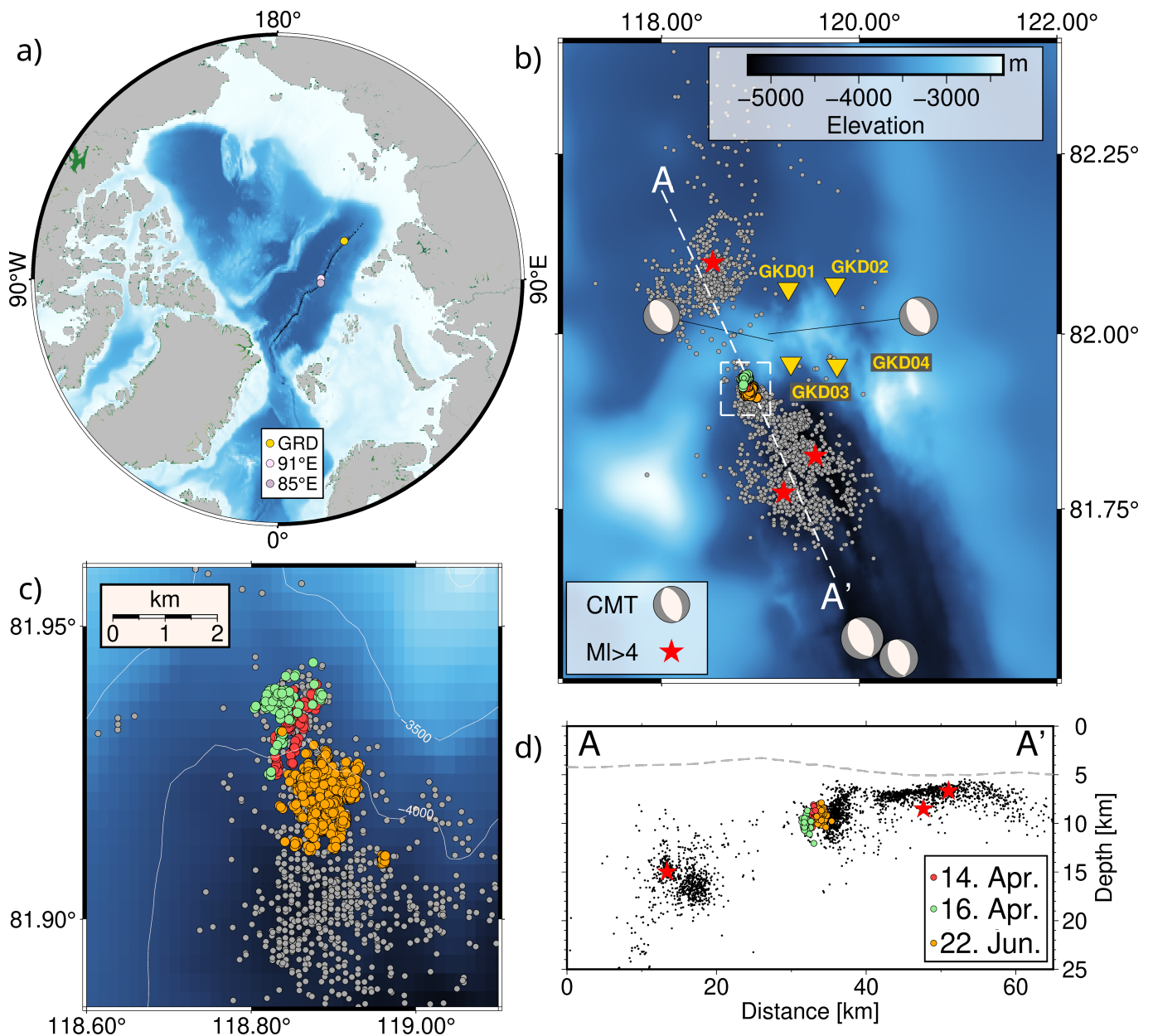


Figure 1 (a) Arctic Ocean with surrounding landmasses. Gakkel Ridge highlighted in black. Location of the study region Gakkel Ridge Deep (GRD). Location where Ding et al. (2022) extracted the velocity model is indicated (91°E), along with the location of the 85°E volcanic complex. (b) Gakkel Ridge Deep with focal mechanisms of the largest earthquakes since 1973 (Ekström et al., 2012). Bathymetry: Jakobsson et al. (2020). Triangles: locations of ocean-bottom seismometers. Gray dots: expectation epicenters of 2855 manually picked and located seismic events meeting the quality criteria for template matching (TM). The largest events ($M_l > 4$) are highlighted by red stars. Color-coded dots indicate seismic bursts with temporal organization ($COV > 3$). (c) Close-up of the area of seismic bursts including events additionally detected by TM. For their visualization, spatial noise is added to the expectation epicenters of their template events (Figure S4). (d) Cross-section of the study area as indicated in (b) with depths below the sea surface. We added the maximum depth (4089 m) below the mean sea level of the four stations (Tab. S1) to the event depths of the catalog.

episodes of seismic unrest observed at distance (e.g., Cesca et al., 2023; Müller and Jokat, 2000), hydroacoustically (Dziak et al., 1995, 2004; Fox and Dziak, 1998) or occasionally on the seafloor (Tolstoy et al., 2006) constitute an important window through which the extensive magmatism at mid-ocean ridges can be studied. Analyzing their seismic characteristics and comparing them to well-observed magmatic episodes in comparable tectonic settings helps to understand active seafloor accretion events in absence of in-situ observations of eruptive activity.

In this study we analyze locally recorded seismicity at one of the easternmost volcanic centers of the Gakkel Ridge with spreading rates of 5 mm/y (Kreemer et al., 2014). The volcanic structure forms the northern boundary of the Gakkel Ridge Deep (GRD) (Nikishin et al., 2018). Teleseismically recorded earthquakes indicate extensional faulting (Figure 1b). Schlindwein (2012) reported some clustered seismicity at GRD, however less intense as at 85°E on the Gakkel Ridge (Figure 1a) or at the Segment 8 volcano on the Southwest Indian Ridge, where additional signs of concur-

rent magmatism were detected (Koulakov et al., 2022; Schlindwein and Riedel, 2010; Schmid et al., 2017). The data from the experiment presented in this study revealed intense seismic activity, motivating a systematic analysis of its spatiotemporal characteristics based on a detailed earthquake catalog. Utilizing an initial catalog of manually extracted events, we employ template matching (TM) to search for small magnitude events, which are typically challenging to capture for systematic analysis. This difficulty is further increased in oceanic environments, where both broadband noise from wave action (Webb, 1998) and high-frequency noise from ocean currents (Essing et al., 2021), short-duration events or whale vocalizations (Domel et al., 2023) interfere with the records of small seismic events.

2 Data and Methodology

The dataset was recorded by a network of 4 broad-band ocean-bottom seismometers (OBS) with an interstation distance between ~ 7 and ~ 14 km located on the northern flank of GRD (Figure 1). The continuous recording with a sampling rate of 100 Hz started on 17.09.2018 and lasted until 17.09.2019. After visual screening, local earthquakes detected by at least three stations were extracted. Subsequently, PhaseNet (Zhu and Beroza, 2018) was used to pick phase arrival times of P- and S-phases. All phase picks were manually quality-controlled. After a preliminary location of 4,503 events (see also Essing et al., 2024), we selected 687 well constrained earthquakes with root-mean-square (RMS) traveltimes residuals < 0.1 s and 8 phase readings in a confined area northwest and south of the network to determine station correction terms. The velocity model used, derived from a refraction seismic experiment by Ding et al. (2022, their pos.1) at a neighboring volcanic center located at $\sim 91^\circ$ E of the Gakkel Ridge (Figure 1a), was extended from 12 to 40 km depth with a P-wave velocity of 8.0 - 8.1 km/s. We used interstation S- and P-phase readings (Figure S1) and previous experience in similar geologic settings (c.f. Meier et al., 2021) to select a v_p/v_s ratio of 1.77. Station correction terms were obtained from the average residuals of P- and S-phases at each station using NonLinLoc (Lomax et al., 2000) as location algorithm (Table S1). Pseudo-Wadati diagrams were used to check the effect of the station correction terms (Figure S2). Subsequently, all 4,503 earthquakes were located with these a priori corrections leading to 3,258 events with an RMS < 0.1 s. Location errors are on average 3.9 km horizontally, and 4.5 km in depth, with absolute depth being poorly constrained due to the network geometry. We further estimate the local magnitude following Hutton and Boore (1987) in the implementation in Seisan (Havskov and Ottemoller, 1999; Havskov et al., 2020) with $M_l = \log_{10}(amp) + 1.11 \log_{10}(dist) + 0.00189 dist - 2.09$, where amp are the amplitudes of the Wood Anderson equivalent horizontal components in nm and $dist$ the hypocentral distance in km.

For the subsequent TM approach, we detrend the continuous OBS data and filter between 5 and 49 Hz to target small events with enhanced signal-to-noise ratio (SNR) at higher frequencies (Abercrombie, 2021). For each

manually picked and located earthquake with an RMS < 0.1 s (3,258 events), we extract 2 s time windows centered around the P- and S-phase from the processed continuous data. P-phase windows are extracted from the vertical component of each station, S-phase windows from the two horizontal components. By using the P and S arrival times at four stations with different hypocentral distances, we intrinsically consider the move-out of the seismic events. In case only one phase was picked at a station, we predict the missing phase arrival time based on the existing phase and the origin time using the v_p/v_s ratio (Tab. S2). When no phases are available at a particular station, we predict them by approximating the P- and S-wave velocities using the distance from the input catalog and travel times of the phases at stations with available phase picks. We note that, while this approach may appear too simplistic, later quality control will ensure that only high-quality templates are used for the subsequent TM approach.

We additionally extract a 2 s lasting noise window starting 3 s before the arrival of the P-phase for quality control. At every component, we calculate the SNR by comparing the RMS amplitude within the signal window to that within the noise window. For TM, we only use high-quality templates that meet the previously mentioned criterion of RMS < 0.1 s and additionally contain at least 6 components with an SNR > 3 . This leads to 2,855 seismic events within the initial catalog (expectation hypocenters are shown in Figure 1b) that meet the quality requirements and are subsequently used as templates. We apply the TM algorithm of Beaucé et al. (2017): At each component the similarity between the template waveform and the continuous seismic data is quantified using the correlation coefficient (CC). The CC between the template window and the continuous data is calculated at each sample, considering the arrival time variations at four different stations (i.e., move-out) that we obtain from the manual picks. Then, a stacked CC value across all stations and components is calculated. To avoid including low-quality waveforms, we downweigh the components by a logistic function (Equation S1) that takes into account the estimated SNR of each component (Duverger et al., 2018). Subsequently all weighted CC values are stacked for the entire network. For each template, this procedure yields a daily time series of stacked CC values, from which we estimate its median absolute deviation (MAD). Based on this statistical measure, we extract new detections at every sample where the stacked CC value is significantly larger than the MAD, and thereby similar to the waveforms of the template (Beaucé et al., 2017). After a visual quality control of the waveforms of new detections (Figure S3), we declare a new detection at every sample that exceeds 11 times the MAD, in agreement with previous studies (Shelly, 2020; Sánchez-Reyes et al., 2021).

For TM, we use all 2,855 events that meet the previously described quality criteria as templates. Templates that share similar waveforms (i.e., similar locations and focal mechanisms) tend to detect similar new events. These multi-detections of single events by different templates have inter-event times < 1 s. To elim-

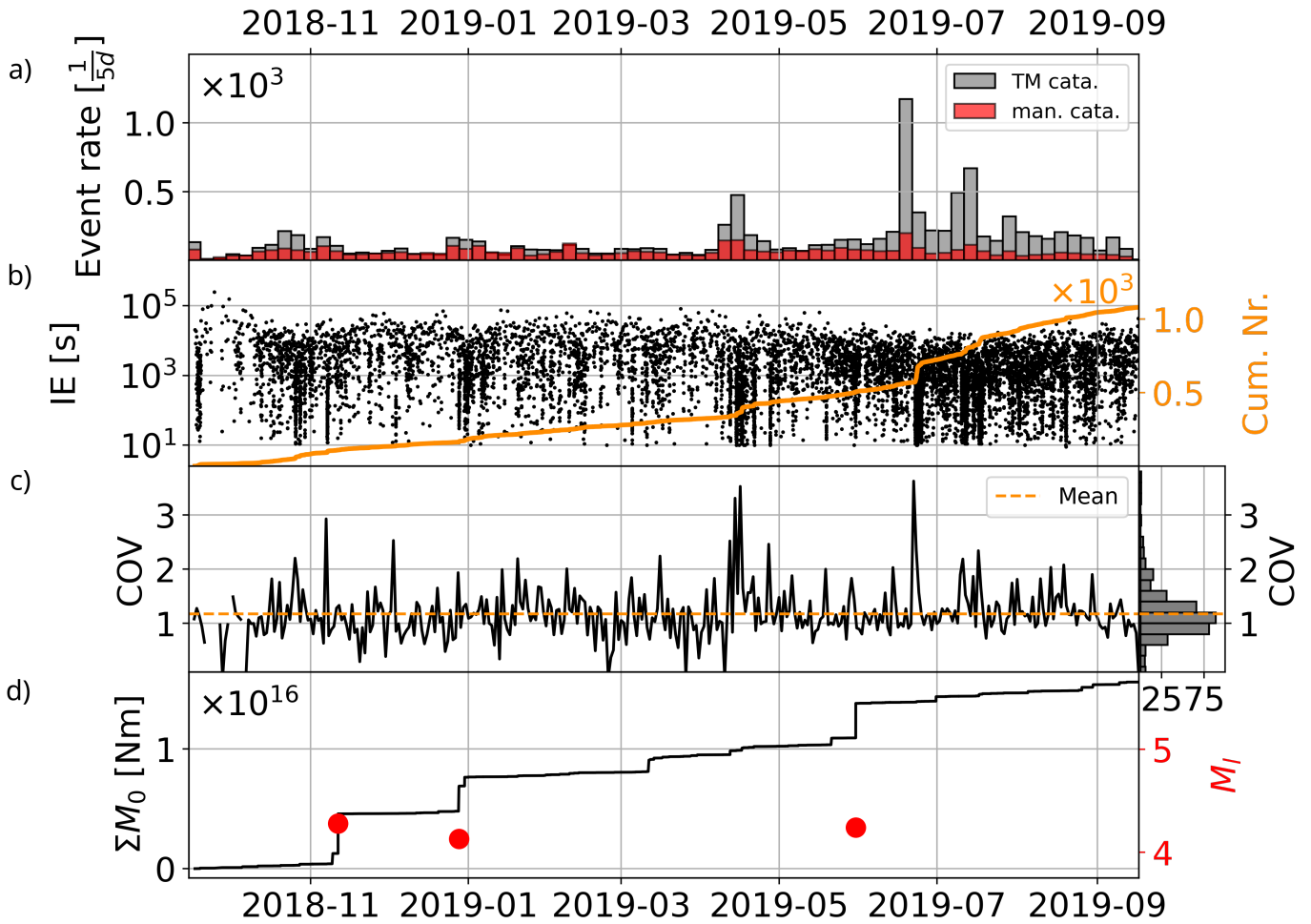


Figure 2 (a) Number of events for time intervals of 5 days for the manually (man.) picked (red) and the enhanced template matching (TM) catalog (gray). (b) Interevent times (IE) and cumulative number of events as a function of time. (c) Daily estimates of the coefficient of variation (COV) of the IE. Note that values below 1 primarily occur on days with a small number of observations. (d) Cumulative seismic moment (M_0). Events with $M_1 > 4$ are marked (red dots).

inate redundant multi-detections from the TM results, we filter the earthquake catalog by requiring a new detection to be separated by a minimum of 10 s from other detections. Within groups of multi-detections, we keep the event with the largest similarity to the template. In cases where multi-detections contain the self-detection of a template, we keep the template as part of the manual catalog, as it has the highest similarity (i.e., correlation coefficient = 1). From a number of 244,591 detections, including all redundant multi-detections, filtering reduces the number to 10,801 detections which includes the 2,855 events that were used as templates.

For each newly detected event we estimate the local magnitude (M_l) following Cabrera et al. (2022). We relate the mean of the absolute amplitude within the template window to the mean of the absolute amplitude of the newly detected event. This is done for each component, and the resulting median across all components is used to estimate M_l . The basic principle is that a decrease in amplitude of a factor of 10 corresponds to a decrease of M_l by a factor of 1 (e.g. Cabrera et al., 2022; Sánchez-Reyes et al., 2021). Finally, we assume M_l to be equivalent to M_w (Roland and McGuire, 2009) and calculate the seismic moment M_0 in Nm as $M_0 = 10^{1.5 \cdot M_l + 9.1}$ (Hanks and Kanamori, 1979).

3 Results

3.1 Performance of TM

The earthquake catalog consists of 2,855 manually picked and located seismic events fulfilling the minimum quality criteria (Figure 1) enriched by 7,946 events automatically extracted by TM (Figure 2a). This corresponds to an extension by a factor of ~ 3 and is primarily attributed to the inclusion of events as small as $M_1 \sim -1$ (Figure 3) resulting in a lower magnitude of completeness of the enhanced catalog.

The temporal distribution of manually picked seismic events (Figure 2a) shows a relatively constant number of events, with occasional bursts of seismicity (e.g., April, June, July 2019).

This trend is consistent with the TM catalog, which typically has barely more detections. However, notable variations between the two catalogs emerge during bursts of seismicity, when the TM catalog has a significant increase in detections. In addition, TM detections increase during the months June–November (Figure 2a), which coincides with a decrease in the ambient noise level in the frequency band 5–49 Hz during summer when sea ice becomes mechanically too weak

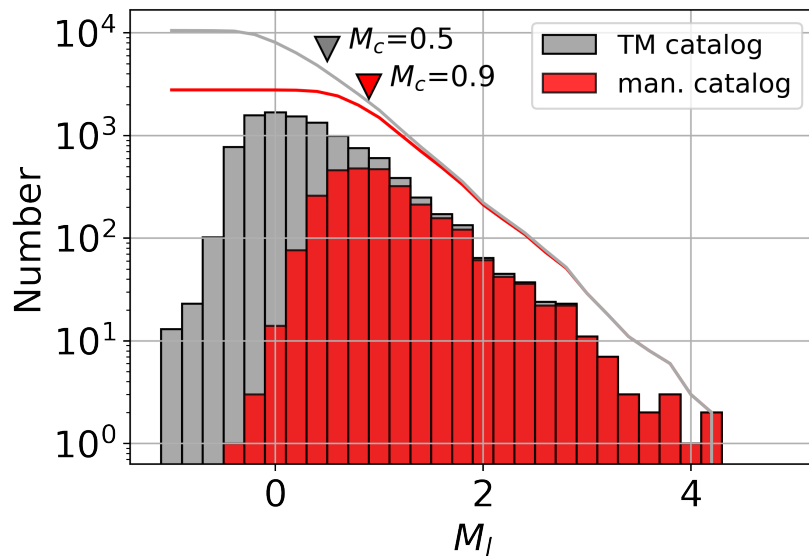


Figure 3 Frequency-magnitude distribution and cumulative number of events based on the estimated local magnitudes (M_l) of the template matching (TM) and the manually (man.) picked earthquake catalogs. The according magnitude of completeness (M_c) is estimated following the Goodness-of-Fit test (Wiemer and Wyss, 2000). Note the additional low magnitude events in the TM catalog compared to the manual catalog.

to break and is no longer under compression (Figure 4). This suggests that the detection capability of TM depends on seasonal variations of the background noise (e.g., Sánchez-Reyes et al., 2021), rather than reflecting temporal variations in the generation of earthquakes.

The time intervals between consecutive events (interevent times (IE), Figure 2b), reflect the high temporal resolution of the catalog with IE reaching down to the smallest temporal separation of 10 s that served as cut-off criterion for multi-detections.

3.2 Temporal seismicity pattern

The cumulative number of the 10,801 seismic events over time (Figure 2b) suggests a largely constant event rate that is occasionally interrupted by short periods of increased activity. To quantify the temporal organization of the seismicity, we exploit the coefficient of variation (COV) of the IEs (Figure 2c). It is defined as ratio of the standard deviation σ to the mean μ and provides information about the distribution of IE between earthquakes (e.g. Essing and Poli, 2024; Kagan and Jackson, 1991). During most days, values fluctuate at ~ 1 , indicating the method's robustness against temporal variations in the detection capability and a Poissonian-like distribution of the IE, hence largely random occurrence of seismicity in time.

Based on the temporal organization, we can thus distinguish between two types of seismicity:

1) Seismicity characterized by irregular event occurrence with IEs between 1,000 and 10,000 s modulated by the temporal variations of the detection capability. Earthquakes occur independently of each other (COV ~ 1). Large magnitude seismic events ($M_l > 4$) causing a step in cumulative moment release belong to this group (Figure 2d). These events appear not to be accompanied by pronounced aftershock sequences that would be expected to deviate from a Poissonian behavior.

2) Bursts of seismicity visible as several sharp vertical lines with significantly lower IEs of 10 - 1,000 s and higher event rates. These peaks coincide with elevated COV values. Three significant peaks (COV > 3) occur on April 14 and 16 and June 22 (Figure 2c), respectively. Their temporal organization deviates strongly from a Poissonian assumption of independent seismic events. Yet, none of these periods of temporally organized seismicity yield a significant increase of moment release or large-magnitude ($M_l > 4$) seismic events (Figure 2d).

3.3 Spatial seismicity pattern

Seismic events are broadly scattered in the valley of the Gakkel Ridge northwest and south of the seismic network with a general increase of depth towards NW (Figures 1b, d). Most of this scattered seismicity belongs to the first group of irregularly occurring earthquakes. In the center, there is a prominent area devoid of seismic activity despite the proximity to the seismic network. The southern termination of this topographically elevated, mostly aseismic area shows numerous, densely clustered seismic events in a confined area (Figures 1c, d) containing the bursts of seismicity, characterized by a COV > 3 . These bursts include numerous TM-detected events that are too weak to be located. However, since they share highly similar waveforms (Figure S3) and move-out characteristics with their detecting template it can be assumed that they originate from the same region (Essing and Poli, 2022). For visualization of the TM-detected events in Figure 1c (not relocated), we add spatial noise to the epicenter location of their detecting template, simulating the collocation of these events (Figure S4).

To reveal potential signs of spatial migration within the seismicity bursts (COV > 3) we use the time differences between the S- and P-phase arrivals as indicator for the distance to the source from station GKD03. We

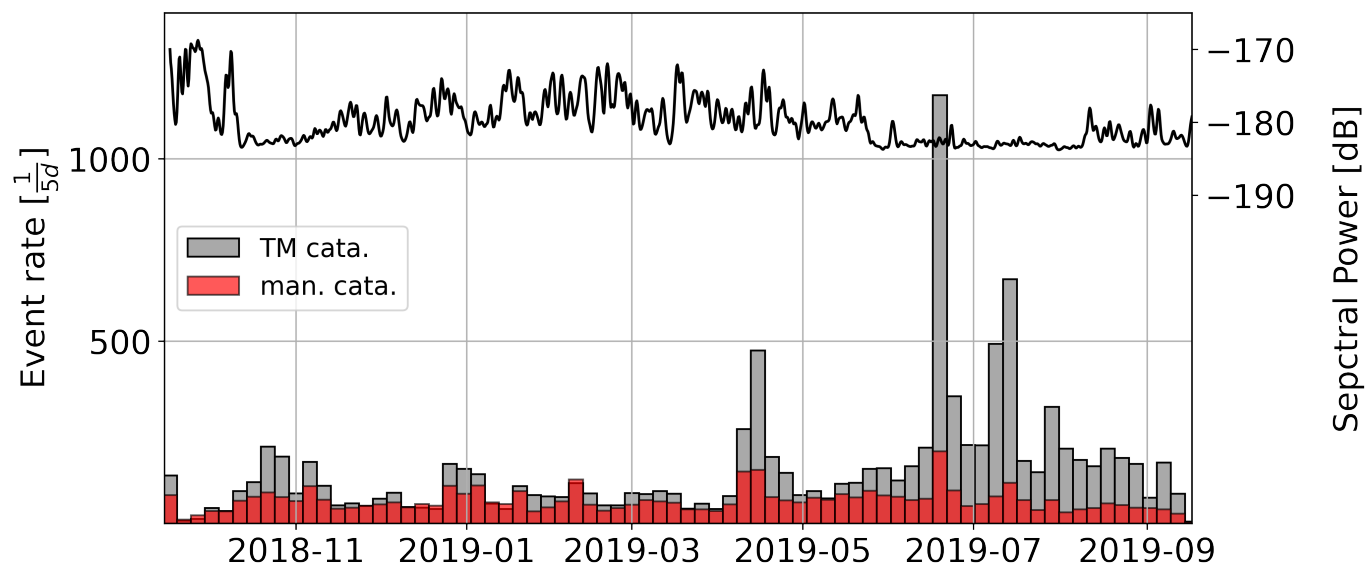


Figure 4 Number of events for time intervals of 5 days for the manually (man.) picked (red) and the enhanced template matching (TM) catalog (gray). Black: Ambient noise level at frequencies of 5 - 49 Hz estimated for component GKD03.HHZ: Power spectra were derived by averaging spectra (65.5 s time windows; overlap 10%) in 30 min bins. Spectral power in the frequency band 5 - 49 Hz was then extracted and averaged and the resulting time series smoothed by a cosine filter with full width of 2 days.

use the manually picked P- and S- phases at this station and cross-correlate each of the two phases with the phases of a TM detection. We align the P-phase and determine the shift that is needed for optimal correlation between the S-phases. The shift is subsequently added to the template's S-P time (Figure 5). This analysis is done only for TM detections that are highly similar to their detecting template ($CC > 0.9$, Poli et al., 2021).

The first seismic burst (April 14, Figure 5a) starts with S-P times of ~ 1.2 s. As the seismicity intensified, the S-P times are 1.15 - 1.3 s. After only 6 h, the event rate fades. The second seismic burst (April 16, Figure 5a) starts with an increase of the seismicity rate at S-P times of 1.25 s. Again, the seismicity spreads out spatially with S-P times between 1.2 s and 1.35 s. During this period, the largest events ($M_l = 3.0$) occur followed by a quick decay in seismicity rate and a total duration of about 11 h. The similar size of the two largest events, together with the fact that they occur several hours after the onset of the burst of seismicity suggests swarm-like behavior. The general increase in S-P times of the two bursts suggests the activation of more distant areas over time, most likely related to a downward migration (Figure 1d, Figure S5).

The third burst of seismicity (June 22-24, Figure 5b) exhibits a long time period of growing event rates before reaching the maximum. During this time, S-P times grow from 1.15 s to 1.28 s, thus increasingly activating more distant areas (see Figure S5). The two largest events have a similar size ($M_l = 2.5$) and occur several hours after the onset of the burst, indicating swarm-like behavior over a duration of 30 h.

4 Interpretation and Discussion

Our experiment with OBSs beneath the perennial sea ice cover of the Arctic Ocean gives insights into the ac-

tive spreading processes at the globally lowest spreading rates. Very little direct observations or petrological sampling at such slow spreading rates exist, in particular since the sediment cover of Gakkel Ridge increases eastwards with the proximity to the Laptev Shelf and decreasing spreading rates (Coakley and Cochran, 1998; Nikishin et al., 2018). The relative role of magmatic and tectonic spreading is largely unknown. Evidence for magmatic processes at GRD exists as volcanic cones at the seafloor and highly reflective units embedded in the sediments, while tectonic graben formation and faulting of overlying sediments is observed further east (Nikishin et al., 2018). Our network, situated in international waters just off the rift axis at the northern rim of GRD, was not optimally positioned for monitoring the previously unknown local seismicity in space. We therefore rely mostly on the temporal characteristics of seismicity to reveal active spreading processes. The resolution of our refined earthquake catalog with detection capabilities down to magnitudes $M_l \sim 0$ (Figure 3) is comparable to earthquake catalogs from onshore experiments in Iceland (Ágústsdóttir et al., 2019) and allows to discuss our results in context with well observed spreading episodes.

We propose that the first group of seismic events scattered in space and without obvious temporal organization ($COV \sim 1$) reflects continuous and ubiquitous tectonic stress release. The moment release is not constant in time, exhibiting occasional $M_l > 4$ earthquakes indicating the presence of larger fault planes. However, seismicity is not confined to distinct fault planes, even during aftershock sequences, which contain relatively few events in the study area. Comparably diffuse seismicity confined to the rift valley also characterizes the ultraslow spreading Knipovich (Meier et al., 2021) and Southwest Indian Ridge (Schmid and Schlindwein, 2016; Schmid et al., 2017; Yu et al., 2018). The spatial loca-

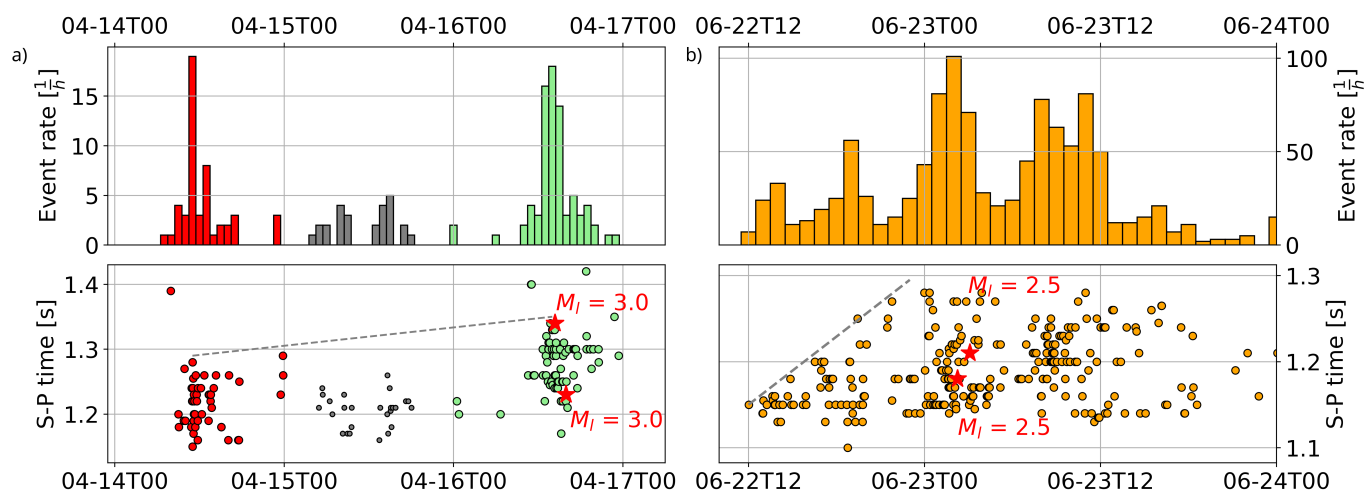


Figure 5 Event rate and time differences between the S- and P-phase arrivals (S-P time) at station GKD03 for bursts in (a) April and (b) June 2019. Red stars: The two largest events of each time window and their M_l . Colors as in Figure 1.

tion accuracy and therefore the potential to resolve individual faults is limited in our study, but networks with similar instrument spacing were able to resolve the seismic activity of individual faults, especially when stress release is focused on large detachment-type faults (Tao et al., 2020).

The spatial extent of the scattered seismicity is not only limited by the rift valley walls, but also controlled by the thermal structure of the lithosphere. We suggest that the aseismic region interrupting the diffuse seismicity results from elevated temperatures that prevent brittle faulting. Meier et al. (2022) and Schmid et al. (2017) observed similar aseismic regions coinciding with the axial highs of volcanic centers (Figures 6b, c). In addition, they obtained high v_p/v_s ratios from local earthquake tomography, suggesting the presence of melt. Earthquake swarms, partly with signs of migration, occur at the margin or partly within these aseismic zones with outward propagation directions, repeatedly occupying the same locations (Meier et al., 2022, 2021). The same spatial relation of the aseismic zone and the bursts of seismicity is observed in the study area (Figures 6a, b). The occurrence of similar-sized largest events late in the bursts (Figure 5) suggests swarm behavior rather than mainshock-aftershock sequences (Båth, 1965). In addition, the distinctly different spatiotemporal characteristics of the bursts compared to the diffuse seismicity suggests a different physical generation process. No geodetic or visual observations exist in these remote locations that could confirm dike intrusions or effusive activity. However, the character of the bursts is similar to Icelandic diking episodes, although even within Iceland, the seismicity accompanying dike intrusions varies, mostly due to the pre-existing stresses that govern the size and focal mechanisms of earthquakes triggered by dike intrusions (Pedersen et al., 2007; Sigmundsson et al., 2024, 2022). The Krafla system is most similar to the orthogonal spreading at GRD. During the 1975 - 84 rifting episode, earthquake swarms with limited release of seismic moment propagated away from an aseismic caldera along the same paths with 2-3 diking events per year (Wright et al.,

2012; Einarsson and Brandsdottir, 1978) covering a distance of few km to 70 km.

By analogy we interpret the axial high forming the northern rim of the GRD as a volcanic center with ongoing magmatism. The ridge section to the north shows a colder lithosphere that is deforming mostly tectonically with diffuse seismicity extending to depths of about 20 km. To the south, in contrast, irregularly occurring earthquake swarms probably indicate intrusions toward the GRD, where generally shallower seismicity is present, and volcanic structures have been identified at the sea floor (Nikishin et al., 2018). The earthquake swarm in June shows hypocenters that are migrating towards the GRD (Figure S5) and the June swarm itself activated a narrow corridor towards GRD in prolongation of the April swarms. In addition, a pronounced circular positive magnetic anomaly, characteristic of volcanic centers at ultraslow spreading ridges (Schlindwein, 2012; Schlindwein and Schmid, 2016), coincides with the aseismic area (Figure 6d), suggesting the presence of a basaltic layer. The swarms observed during our experiment extended a maximum of 4 km towards GRD where the seismicity becomes diffuse and spreads out spatially. Here, only a weakly positive central magnetic anomaly is visible. The Logachev volcanic center of the Knipovich Ridge shows similar dimensions of the aseismic area together with swarm activity restricted to its vicinity. Meanwhile the Segment 8 volcano at the South West Indian Ridge is surrounded by a larger aseismic area and potentially related swarm activity spreads out far into the segment comparable to the Krafla system.

However, we cannot rule out that hydrothermal fluids instead of magma cause the swarm activity. Flóvenz et al. (2022) describe low-level seismicity occurring in swarms above a hot area on the Reykjanes Peninsula in Iceland. Geodetic modelling suggests that fluid intrusions into an aquifer cause the seismicity. Tolstoy et al. (2008) observed shallow, weak seismicity on top of an axial magma chamber at the East Pacific Rise and attribute this seismicity to hydrothermal circulation. Both these cases are still related to concurrent

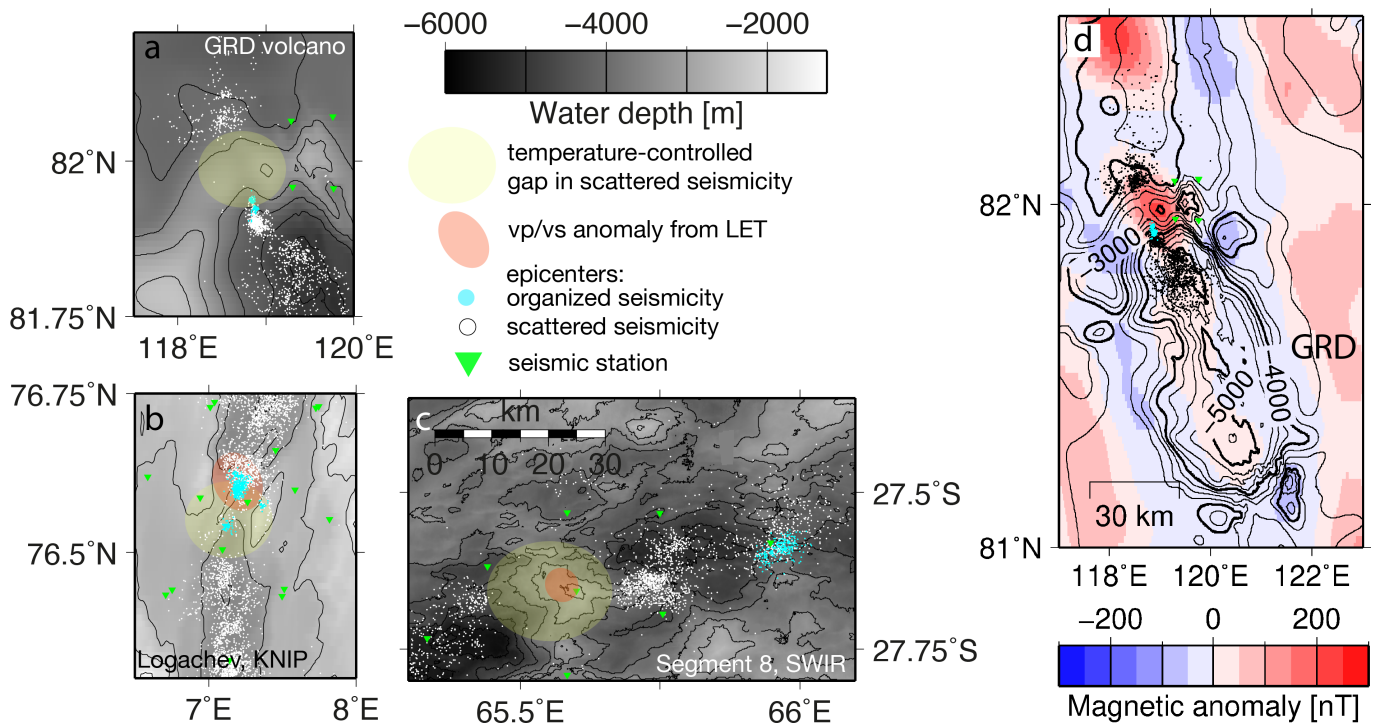


Figure 6 Relative positions of seismicity, gaps in seismicity and increased v_p/v_s ratios from local earthquake tomography at (a) Gakkel Ridge Deep (GRD), quality threshold for shown events: $RMS < 0.1$ s (after station correction) and 8 phases, (1,594 of 4,503 initial events, see also [Essing et al., 2024](#)), (b) Logachev volcano at the Knipovich Ridge (KNIP) (KNIP, [Meier et al., 2022](#), quality threshold for shown events: depth error < 5 km), (c) the Segment 8 volcano at the Southwest Indian Ridge (SWIR, [Schmid et al., 2017](#), quality threshold for shown events: depth error < 5 km). (d) Total magnetic anomaly at GRD ([Gaina et al., 2011](#)).

magmatism. They differ from our setting as the seismicity is triggered on top of a heated area rather than at its margin, with a tendency of migration away from the heat source. We therefore suggest that the observed swarm activity near the GRD is related to ongoing magmatism and likely reflects diking activity or injection of heated fluids.

The seismological signs for active magmatism at spreading rates as low as 5 mm/y and the similarity to the seismicity of volcanic centers at higher spreading rates (Logachev 11.7 mm/y; 9 mm/y effective spreading rate, Segment 8: 13.5 mm/y, [Kreemer et al., 2014](#)) support the findings of [O'Connor et al. \(2021\)](#) that discontinuous volcanism is present along the entire Gakkel Ridge and is characteristic of ultraslow spreading independently of the actual ultraslow spreading rate. However, the individual volcanic centers of Gakkel Ridge may display different forms of seismic and volcanic activity: The 85°E volcanic complex produced the largest teleseismically registered earthquake swarm lasting over a period of 9 months in 1999 ([Müller and Jokat, 2000](#); [Schlindwein, 2012](#); [Tolstoy et al., 2001](#)), clearly differing in size, magnitude and duration from the seismicity observed at GRD both locally and at teleseismic distances. Seafloor imagery revealed signs of unusual explosive activity at 85°E ([Sohn et al., 2008](#)). Comparable seafloor imagery does not exist for the GRD volcano, such that we cannot confirm that the different character of the seismic activity is an expression of a different style of volcanic activity. However, with newly de-

veloped ocean bottom seismometers suitable for operations in sea ice and a generally receding sea ice coverage in the Arctic Ocean, a more systematic investigation of ultraslow spreading processes becomes possible ([Ding et al., 2022](#); [Schlindwein, 2023](#)).

5 Conclusion

Despite difficult circumstances due to sea ice coverage and remote location, the deployment of a small OBS array at GRD combined with modern detection methods revealed two distinct types of seismicity: a) randomly occurring seismicity scattered in the rift valley and b) highly organized seismicity confined to a narrow area at the margin of an aseismic zone. While the first type is likely related to tectonic processes, the second type exhibits characteristics similar to seismicity during dyke intrusions in magmatic environments. The prominent GRD is thus bounded by a presumably active volcanic center with localized magmatism, evidenced also by a circular magnetic anomaly and a temperature-controlled gap in the scattered seismicity. The similarity in seismic activity patterns among three distinct volcanic centers located at ultraslow spreading ridges indicates that discontinuous and highly focused magmatism plays an important role in the process of crustal accretion occurring at extremely low rates of spreading.

Acknowledgements

DE acknowledges the Helmholtz Information & Data Science Academy (HIDA) for financial support for a short-term research stay at the Alfred-Wegener-Institute, Helmholtz Centre for Polar and Marine Research. Ship time on RV Polarstern was provided under grant AWI_PS115/2_01. OBS were obtained from the DEPAS instrument pool (Alfred-Wegener-Institut, 2017). We sincerely thank the editor, Lise Retailleau, Jean-Marie Saurel, and an anonymous reviewer for their time and constructive feedback, which helped to improve the manuscript.

6 Data and code availability

Maps were created using GMT 6.0 (Wessel et al., 2019) and PyGMT (Uieda et al., 2021). Seismic data were processed with ObsPy (Beyreuther et al., 2010). TM was realized using FMF (Beaucé et al., 2017) available at https://github.com/beridel/fast_matched_filter. Raw, continuous seismic data are available from PANGAEA (Schlindwein et al., 2022b), time-corrected miniseed data from GEOFON network code 8F (Schlindwein et al., 2022a). Computations were performed using the AWI High-Performance Computing infrastructure ALBEDO (<https://www.awi.de/en/about-us/service/computing-centre.html>). Earthquake catalogs produced in this study are available at Essing et al. (2024) and can be provided in other formats upon request.

7 Competing interests

The authors acknowledge that to their knowledge there are no conflicts of interest.

References

Abercrombie, R. E. Resolution and uncertainties in estimates of earthquake stress drop and energy release. *Philosophical Transactions of the Royal Society A: Mathematical, Physical and Engineering Sciences*, 379(2196):20200131, Mar. 2021. doi: 10.1098/rsta.2020.0131.

Ágústsdóttir, T., Woods, J., Greenfield, T., Green, R. G., White, R. S., Winder, T., Brandsdóttir, B., Steinhórnsson, S., and Soosalu, H. Strike-slip faulting during the 2014 Bárðarbunga-Holuhraun dike intrusion, central Iceland. *Geophysical Research Letters*, 43(4):1495–1503, Feb. 2016. doi: 10.1002/2015gl067423.

Ágústsdóttir, T., Winder, T., Woods, J., White, R. S., Greenfield, T., and Brandsdóttir, B. Intense Seismicity During the 2014–2015 Bárðarbunga-Holuhraun Rifting Event, Iceland, Reveals the Nature of Dike-Induced Earthquakes and Caldera Collapse Mechanisms. *Journal of Geophysical Research: Solid Earth*, 124(8): 8331–8357, Aug. 2019. doi: 10.1029/2018jb016010.

Beaucé, E., Frank, W. B., and Romanenko, A. Fast Matched Filter (FMF): An Efficient Seismic Matched-Filter Search for Both CPU and GPU Architectures. *Seismological Research Letters*, 89(1): 165–172, Dec. 2017. doi: 10.1785/0220170181.

Bergman, E. A. and Solomon, S. C. Earthquake swarms on the Mid-Atlantic Ridge: Products of magmatism or extensional tectonics? *Journal of Geophysical Research: Solid Earth*, 95(B4): 4943–4965, Apr. 1990. doi: 10.1029/jb095ib04p04943.

Beyreuther, M., Barsch, R., Krischer, L., Megies, T., Behr, Y., and Wassermann, J. ObsPy: A Python Toolbox for Seismology. *Seismological Research Letters*, 81(3):530–533, May 2010. doi: 10.1785/gssrl.81.3.530.

Båth, M. Lateral inhomogeneities of the upper mantle. *Tectonophysics*, 2(6):483–514, Dec. 1965. doi: 10.1016/0040-1951(65)90003-x.

Cabrera, L., Poli, P., and Frank, W. B. Tracking the Spatio-Temporal Evolution of Foreshocks Preceding the Mw 6.1 2009 L'Aquila Earthquake. *Journal of Geophysical Research: Solid Earth*, 127(3), Mar. 2022. doi: 10.1029/2021jb023888.

Cannat, M., Sauter, D., Mendel, V., Ruellan, E., Okino, K., Escartin, J., Combier, V., and Baala, M. Modes of seafloor generation at a melt-poor ultraslow-spreading ridge. *Geology*, 34(7):605, 2006. doi: 10.1130/g22486.1.

Cesca, S., Metz, M., Büyükakpınar, P., and Dahm, T. The Energetic 2022 Seismic Unrest Related to Magma Intrusion at the North Mid-Atlantic Ridge. *Geophysical Research Letters*, 50(13), July 2023. doi: 10.1029/2023gl102782.

Coakley, B. J. and Cochran, J. R. Gravity evidence of very thin crust at the Gakkel Ridge (Arctic Ocean). *Earth and Planetary Science Letters*, 162(1–4):81–95, Oct. 1998. doi: 10.1016/s0012-821x(98)00158-7.

Ding, W., Niu, X., Zhang, T., Chen, S., Liu, S., Tan, P., Kong, F., Jin, Z., Huang, S., Wei, C., Fang, Y., Sun, Q., and Li, J. Submarine wide-angle seismic experiments in the High Arctic: The JASMinE Expedition in the slowest spreading Gakkel Ridge. *Geosystems and Geoenvironment*, 1(3):100076, Aug. 2022. doi: 10.1016/j.geogeo.2022.100076.

Domel, P., Hibert, C., Schlindwein, V., and Plaza-Faverola, A. Event recognition in marine seismological data using Random Forest machine learning classifier. *Geophysical Journal International*, 235(1):589–609, May 2023. doi: 10.1093/gji/ggad244.

Duverger, C., Lambotte, S., Bernard, P., Lyon-Caen, H., Deschamps, A., and Necessian, A. Dynamics of microseismicity and its relationship with the active structures in the western Corinth Rift (Greece). *Geophysical Journal International*, 215(1):196–221, June 2018. doi: 10.1093/gji/ggy264.

Dziak, R. P., Fox, C. G., and Schreiner, A. E. The June–July 1993 seismo-acoustic event at CoAxial segment, Juan de Fuca Ridge: Evidence for a lateral dike injection. *Geophysical Research Letters*, 22(2):135–138, Jan. 1995. doi: 10.1029/94gl01857.

Dziak, R. P., Smith, D. K., Bohnenstiehl, D. R., Fox, C. G., Desbruyeres, D., Matsumoto, H., Tolstoy, M., and Fornari, D. J. Evidence of a recent magma dike intrusion at the slow spreading Lucky Strike segment, Mid-Atlantic Ridge. *Journal of Geophysical Research: Solid Earth*, 109(B12), Dec. 2004. doi: 10.1029/2004jb003141.

Einarsson, P. and Brandsdóttir, B. *Seismological evidence for Lateral magma intrusion during the July 1978 deflation of the Krafla volcano in NE-Iceland*. July 1978. doi: 10.2172/890964.

Ekström, G., Nettles, M., and Dziewoński, A. The global CMT project 2004–2010: Centroid-moment tensors for 13,017 earthquakes. *Physics of the Earth and Planetary Interiors*, 200–201:1–9, June 2012. doi: 10.1016/j.pepi.2012.04.002.

Escartín, J., Smith, D. K., Cann, J., Schouten, H., Langmuir, C. H., and Escrig, S. Central role of detachment faults in accretion of slow-spreading oceanic lithosphere. *Nature*, 455(7214): 790–794, Oct. 2008. doi: 10.1038/nature07333.

Essing, D. and Poli, P. Spatiotemporal Evolution of the Seismicity in the Alto Tiberina Fault System Revealed by a High-Resolution Template Matching Catalog. *Journal of Geophysical Research: Solid Earth*, 127(10), Oct. 2022. doi: 10.1029/2022jb024845.

- Essing, D. and Poli, P. Unraveling Earthquake Clusters Composing the 2014 Alto Tiberina Earthquake Swarm via Unsupervised Learning. *Journal of Geophysical Research: Solid Earth*, 129(1), Jan. 2024. doi: 10.1029/2022jb026237.
- Essing, D., Schlindwein, V., Schmidt-Aursch, M. C., Hadziioannou, C., and Stähler, S. C. Characteristics of Current-Induced Harmonic Tremor Signals in Ocean-Bottom Seismometer Records. *Seismological Research Letters*, 92(5):3100–3112, Apr. 2021. doi: 10.1785/0220200397.
- Essing, D., Schlindwein, V., and Hellbrück, A. Earthquake Catalog and Phase-Picks from Gakkel Ridge Deep, 2024. doi: 10.5281/ZENODO.11261315.
- Flóvenz, Ó.G., Wang, R., Hersir, G. P., Dahm, T., Hainzl, S., Vassileva, M., Drouin, V., Heimann, S., Isken, M. P., Gudnason, E. Ó. Ágústsson, K., Ágústsdóttir, T., Horálek, J., Motagh, M., Walter, T. R., Rivalta, E., Jousset, P., Krawczyk, C. M., and Milkereit, C. Cyclical geothermal unrest as a precursor to Iceland's 2021 Fagradalsfjall eruption. *Nature Geoscience*, 15(5):397–404, May 2022. doi: 10.1038/s41561-022-00930-5.
- Fox, C. G. and Dziak, R. P. Hydroacoustic detection of volcanic activity on the Gorda Ridge, February–March 1996. *Deep Sea Research Part II: Topical Studies in Oceanography*, 45(12):2513–2530, Dec. 1998. doi: 10.1016/s0967-0645(98)00081-2.
- Gaina, C., Werner, S. C., Saltus, R., and Maus, S. Chapter 3 Circum-Arctic mapping project: new magnetic and gravity anomaly maps of the Arctic. *Geological Society, London, Memoirs*, 35(1):39–48, Jan. 2011. doi: 10.1144/m35.3.
- Hanks, T. C. and Kanamori, H. A moment magnitude scale. *Journal of Geophysical Research: Solid Earth*, 84(B5):2348–2350, May 1979. doi: 10.1029/jb084ib05p02348.
- Havskov, J. and Ottemoller, L. SeisAn Earthquake Analysis Software. *Seismological Research Letters*, 70(5):532–534, Sept. 1999. doi: 10.1785/gssrl.70.5.532.
- Havskov, J., Voss, P. H., and Ottemöller, L. Seismological Observatory Software: 30 Yr of SEISAN. *Seismological Research Letters*, 91(3):1846–1852, Mar. 2020. doi: 10.1785/0220190313.
- Hutton, L. K. and Boore, D. M. The Ml scale in Southern California. *Bulletin of the Seismological Society of America*, 77(6):2074–2094, Dec. 1987. doi: 10.1785/bssa0770062074.
- Jakobsson, M., Mayer, L. A., Bringensparr, C., Castro, C. F., Mohammad, R., Johnson, P., Ketter, T., Accetella, D., Amblas, D., An, L., Arndt, J. E., Canals, M., Casamor, J. L., Chauché, N., Coakley, B., Danielson, S., Demarte, M., Dickson, M.-L., Dorschel, B., Dowdeswell, J. A., Dreutter, S., Fremand, A. C., Gallant, D., Hall, J. K., Hehemann, L., Hodnesdal, H., Hong, J., Ivaldi, R., Kane, E., Klaucke, I., Krawczyk, D. W., Kristoffersen, Y., Kuipers, B. R., Millan, R., Masetti, G., Morlighem, M., Noormets, R., Prescott, M. M., Rebesco, M., Rignot, E., Semiletov, I., Tate, A. J., Travaglini, P., Velicogna, I., Weatherall, P., Weinrebe, W., Willis, J. K., Wood, M., Zarayskaya, Y., Zhang, T., Zimmermann, M., and Zinglarsen, K. B. The International Bathymetric Chart of the Arctic Ocean Version 4.0. *Scientific Data*, 7(1), July 2020. doi: 10.1038/s41597-020-0520-9.
- Kagan, Y. Y. and Jackson, D. D. Long-Term Earthquake Clustering. *Geophysical Journal International*, 104(1):117–134, Jan. 1991. doi: 10.1111/j.1365-246x.1991.tb02498.x.
- Koulakov, I., Schlindwein, V., Liu, M., Gerya, T., Jakovlev, A., and Ivanov, A. Low-degree mantle melting controls the deep seismicity and explosive volcanism of the Gakkel Ridge. *Nature Communications*, 13(1), June 2022. doi: 10.1038/s41467-022-30797-4.
- Kreemer, C., Blewitt, G., and Klein, E. C. A geodetic plate motion and Global Strain Rate Model. *Geochemistry, Geophysics, Geosystems*, 15(10):3849–3889, Oct. 2014. doi: 10.1002/2014gc005407.
- Lomax, A., Virieux, J., Volant, P., and Berge-Thierry, C. *Probabilistic Earthquake Location in 3D and Layered Models*, page 101–134. Springer Netherlands, 2000. doi: 10.1007/978-94-015-9536-0_5.
- Meier, M., Schlindwein, V., Scholz, J., Geils, J., Schmidt-Aursch, M. C., Krüger, F., Czuba, W., and Janik, T. Segment-Scale Seismicity of the Ultraslow Spreading Knipovich Ridge. *Geochemistry, Geophysics, Geosystems*, 22(2), Feb. 2021. doi: 10.1029/2020gc009375.
- Meier, M., Schlindwein, V., and Schmid, F. Magmatic Activity and Dynamics of Melt Supply of Volcanic Centers of Ultraslow Spreading Ridges: Hints From Local Earthquake Tomography at the Knipovich Ridge. *Geochemistry, Geophysics, Geosystems*, 23(10), Oct. 2022. doi: 10.1029/2021gc010210.
- Müller, C. and Jokat, W. Seismic evidence for volcanic activity discovered in central Arctic. *Eos, Transactions American Geophysical Union*, 81(24):265–269, June 2000. doi: 10.1029/00eo00186.
- Nikishin, A., Gaina, C., Petrov, E., Malyshev, N., and Freiman, S. Eurasia Basin and Gakkel Ridge, Arctic Ocean: Crustal asymmetry, ultra-slow spreading and continental rifting revealed by new seismic data. *Tectonophysics*, 746:64–82, Oct. 2018. doi: 10.1016/j.tecto.2017.09.006.
- O'Connor, J. M., Jokat, W., Michael, P. J., Schmidt-Aursch, M. C., Miggins, D. P., and Koppers, A. A. P. Thermochemical anomalies in the upper mantle control Gakkel Ridge accretion. *Nature Communications*, 12(1), Nov. 2021. doi: 10.1038/s41467-021-27058-1.
- Pedersen, R., Sigmundsson, F., and Einarsson, P. Controlling factors on earthquake swarms associated with magmatic intrusions; Constraints from Iceland. *Journal of Volcanology and Geothermal Research*, 162(1–2):73–80, Apr. 2007. doi: 10.1016/j.jvolgeores.2006.12.010.
- Poli, P., Cabrera, L., Flores, M. C., Báez, J. C., Ammirati, J. B., Vásquez, J., and Ruiz, S. Volcanic Origin of a Long-Lived Swarm in the Central Bransfield Basin, Antarctica. *Geophysical Research Letters*, 49(1), Dec. 2021. doi: 10.1029/2021gl095447.
- Roland, E. and McGuire, J. J. Earthquake swarms on transform faults. *Geophysical Journal International*, 178(3):1677–1690, Sept. 2009. doi: 10.1111/j.1365-246x.2009.04214.x.
- Rubin, A. M. and Gillard, D. Dike-induced earthquakes: Theoretical considerations. *Journal of Geophysical Research: Solid Earth*, 103(B5):10017–10030, May 1998. doi: 10.1029/97jb03514.
- Sauter, D., Cannat, M., Rouméjon, S., Andreani, M., Birot, D., Bronner, A., Brunelli, D., Carlut, J., Delacour, A., Guyader, V., MacLeod, C. J., Manatschal, G., Mendel, V., Ménez, B., Pasini, V., Ruellan, E., and Searle, R. Continuous exhumation of mantle-derived rocks at the Southwest Indian Ridge for 11 million years. *Nature Geoscience*, 6(4):314–320, Mar. 2013. doi: 10.1038/ngeo1771.
- Schlindwein, V. Teleseismic earthquake swarms at ultraslow spreading ridges: indicator for dyke intrusions? *Geophysical Journal International*, 190(1):442–456, May 2012. doi: 10.1111/j.1365-246x.2012.05502.x.
- Schlindwein, V. The Expedition PS137 of the Research Vessel POLARSTERN to the Arctic Ocean in 2023. *Reports on Polar Research*, 781(https://doi.org/10.57738/BzPM_0781_2023), 2023.
- Schlindwein, V. and Riedel, C. Location and source mechanism of sound signals at Gakkel ridge, Arctic Ocean: Submarine Strombolian activity in the 1999–2001 volcanic episode. *Geochemistry, Geophysics, Geosystems*, 11(1), Jan. 2010. doi: 10.1029/2009gc002706.
- Schlindwein, V. and Schmid, F. Mid-ocean-ridge seismicity reveals extreme types of ocean lithosphere. *Nature*, 535(7611):276–279,

- June 2016. doi: [10.1038/nature18277](https://doi.org/10.1038/nature18277).
- Schlundwein, V., Kirk, H., Hiller, M., Scholz, J.-R., and Schmidt-Aursch, M. GAKKELDEEP: DEPAS ocean-bottom seismometer operations at the Gakkel Ridge in 2018-2019, 2022a. doi: [10.14470/3S7563492742](https://doi.org/10.14470/3S7563492742).
- Schlundwein, V., Kirk, H., Hiller, M., Scholz, J.-R., and Schmidt-Aursch, M. Project GAKKELDEEP: DEPAS ocean-bottom seismometer operations at the Gakkel Ridge in 2018-2019, 2022b. doi: [10.1594/PANGAEA.947045](https://doi.org/10.1594/PANGAEA.947045).
- Schmid, F. and Schlundwein, V. Microearthquake activity, lithospheric structure, and deformation modes at an amagmatic ultraslow spreading Southwest Indian Ridge segment. *Geochemistry, Geophysics, Geosystems*, 17(7):2905–2921, July 2016. doi: [10.1002/2016gc006271](https://doi.org/10.1002/2016gc006271).
- Schmid, F., Schlundwein, V., Koulakov, I., Plötz, A., and Scholz, J.-R. Magma plumbing system and seismicity of an active mid-ocean ridge volcano. *Scientific Reports*, 7(1), Feb. 2017. doi: [10.1038/srep42949](https://doi.org/10.1038/srep42949).
- Shelly, D. R. A High-Resolution Seismic Catalog for the Initial 2019 Ridgecrest Earthquake Sequence: Foreshocks, Aftershocks, and Faulting Complexity. *Seismological Research Letters*, 91(4): 1971–1978, Jan. 2020. doi: [10.1785/0220190309](https://doi.org/10.1785/0220190309).
- Sigmundsson, F., Parks, M., Hooper, A., Geirsson, H., Vogfjörð, K. S., Drouin, V., Ófeigsson, B. G., Hreinsdóttir, S., Hjaltadóttir, S., Jónsdóttir, K., Einarsson, P., Barsotti, S., Horálek, J., and Ágústsdóttir, T. Deformation and seismicity decline before the 2021 Fagradalsfjall eruption. *Nature*, 609(7927):523–528, Sept. 2022. doi: [10.1038/s41586-022-05083-4](https://doi.org/10.1038/s41586-022-05083-4).
- Sigmundsson, F., Parks, M., Geirsson, H., Hooper, A., Drouin, V., Vogfjörð, K. S., Ófeigsson, B. G., Greiner, S. H. M., Yang, Y., Lanzi, C., De Pascale, G. P., Jónsdóttir, K., Hreinsdóttir, S., Tolpekin, V., Friðriksdóttir, H. M., Einarsson, P., and Barsotti, S. Fracturing and tectonic stress drive ultrarapid magma flow into dikes. *Science*, 383(6688):1228–1235, Mar. 2024. doi: [10.1126/science.adn2838](https://doi.org/10.1126/science.adn2838).
- Sohn, R. A., Willis, C., Humphris, S., Shank, T. M., Singh, H., Edmonds, H. N., Kunz, C., Hedman, U., Helmke, E., Jakuba, M., Liljebladh, B., Linder, J., Murphy, C., Nakamura, K.-i., Sato, T., Schlundwein, V., Stranne, C., Tausenfreund, M., Upchurch, L., Winsor, P., Jakobsson, M., and Soule, A. Explosive volcanism on the ultraslow-spreading Gakkel ridge, Arctic Ocean. *Nature*, 453(7199):1236–1238, June 2008. doi: [10.1038/nature07075](https://doi.org/10.1038/nature07075).
- Sánchez-Reyes, H., Essing, D., Beaucé, E., and Poli, P. The Imbricated Foreshock and Aftershock Activities of the Balsorano (Italy) Mw 4.4 Normal Fault Earthquake and Implications for Earthquake Initiation. *Seismological Research Letters*, 92(3): 1926–1936, Jan. 2021. doi: [10.1785/0220200253](https://doi.org/10.1785/0220200253).
- Tao, C., Seyfried, W. E., Lowell, R. P., Liu, Y., Liang, J., Guo, Z., Ding, K., Zhang, H., Liu, J., Qiu, L., Egorov, I., Liao, S., Zhao, M., Zhou, J., Deng, X., Li, H., Wang, H., Cai, W., Zhang, G., Zhou, H., Lin, J., and Li, W. Deep high-temperature hydrothermal circulation in a detachment faulting system on the ultra-slow spreading ridge. *Nature Communications*, 11(1), Mar. 2020. doi: [10.1038/s41467-020-15062-w](https://doi.org/10.1038/s41467-020-15062-w).
- Tolstoy, M., Bohnenstiehl, D., Edwards, M., and Kurras, G. Seismic character of volcanic activity at the ultraslow-spreading Gakkel Ridge. *Geology*, 29(12):1139, 2001. doi: [10.1130/0091-7613\(2001\)029<1139:scovaa>2.0.co;2](https://doi.org/10.1130/0091-7613(2001)029<1139:scovaa>2.0.co;2).
- Tolstoy, M., Cowen, J. P., Baker, E. T., Fornari, D. J., Rubin, K. H., Shank, T. M., Waldhauser, F., Bohnenstiehl, D. R., Forsyth, D. W., Holmes, R. C., Love, B., Perfit, M. R., Weekly, R. T., Soule, S. A., and Glazer, B. A Sea-Floor Spreading Event Captured by Seismometers. *Science*, 314(5807):1920–1922, Dec. 2006. doi: [10.1126/science.1133950](https://doi.org/10.1126/science.1133950).
- Tolstoy, M., Waldhauser, F., Bohnenstiehl, D. R., Weekly, R. T., and Kim, W.-Y. Seismic identification of along-axis hydrothermal flow on the East Pacific Rise. *Nature*, 451(7175):181–184, Jan. 2008. doi: [10.1038/nature06424](https://doi.org/10.1038/nature06424).
- Uieda, L., Tian, D., Leong, W. J., Toney, L., Schlitzer, W., Grund, M., Newton, T., Ziebarth, M., Jones, M., and Wessel, P. PyGMT: A Python interface for the Generic Mapping Tools, 2021. doi: [10.5281/ZENODO.4522136](https://doi.org/10.5281/ZENODO.4522136).
- Webb, S. Broadband seismology and noise under the ocean. *Reviews of Geophysics*, 36(1):105–142, 1998.
- Wessel, P., Luis, J. F., Uieda, L., Scharroo, R., Wobbe, F., Smith, W. H. F., and Tian, D. The Generic Mapping Tools Version 6. *Geochemistry, Geophysics, Geosystems*, 20(11):5556–5564, Nov. 2019. doi: [10.1029/2019gc008515](https://doi.org/10.1029/2019gc008515).
- Wiemer, S. and Wyss, M. Minimum Magnitude of Completeness in Earthquake Catalogs: Examples from Alaska, the Western United States, and Japan. *Bulletin of the Seismological Society of America*, 90(4):859–869, 08 2000. doi: [10.1785/0119990114](https://doi.org/10.1785/0119990114).
- Wright, T. J., Sigmundsson, F., Pagli, C., Belachew, M., Hamling, I. J., Brandsdóttir, B., Keir, D., Pedersen, R., Ayele, A., Ebinger, C., Einarsson, P., Lewi, E., and Calais, E. Geophysical constraints on the dynamics of spreading centres from rifting episodes on land. *Nature Geoscience*, 5(4):242–250, Mar. 2012. doi: [10.1038/ngeo1428](https://doi.org/10.1038/ngeo1428).
- Yu, Z., Li, J., Niu, X., Rawlinson, N., Ruan, A., Wang, W., Hu, H., Wei, X., Zhang, J., and Liang, Y. Lithospheric Structure and Tectonic Processes Constrained by Microearthquake Activity at the Central Ultraslow-Spreading Southwest Indian Ridge (49.2° to 50.8°E). *Journal of Geophysical Research: Solid Earth*, 123(8): 6247–6262, Aug. 2018. doi: [10.1029/2017jb015367](https://doi.org/10.1029/2017jb015367).
- Zhu, W. and Beroza, G. C. PhaseNet: A Deep-Neural-Network-Based Seismic Arrival Time Picking Method. *Geophysical Journal International*, Oct. 2018. doi: [10.1093/gji/ggy423](https://doi.org/10.1093/gji/ggy423).

The article *Magmatic activity at the slowest spreading rates: insights from a high-resolution earthquake catalog obtained from Gakkel Ridge Deep (Arctic Ocean)* © 2025 by David Essing is licensed under CC BY 4.0.